



AFRL-RX-WP-JA-2017-0470

CASE STUDY OF MODEL-BASED INVERSION OF THE ANGLE-BEAM ULTRASONIC RESPONSE FROM COMPOSITE IMPACT DAMAGE (POSTPRINT)

Laura Homa
University of Dayton Research Institute

John Wertz, John Welter, and Daniel Sparkman
AFRL/RX

John Aldrin
Computational Tools

22 September 2017
Interim Report

Distribution Statement A.
Approved for public release: distribution unlimited.

© 2018 ASME

(STINFO COPY)

AIR FORCE RESEARCH LABORATORY
MATERIALS AND MANUFACTURING DIRECTORATE
WRIGHT-PATTERSON AIR FORCE BASE, OH 45433-7750
AIR FORCE MATERIEL COMMAND
UNITED STATES AIR FORCE

REPORT DOCUMENTATION PAGE				Form Approved OMB No. 0704-0188
<p>The public reporting burden for this collection of information is estimated to average 1 hour per response, including the time for reviewing instructions, searching existing data sources, gathering and maintaining the data needed, and completing and reviewing the collection of information. Send comments regarding this burden estimate or any other aspect of this collection of information, including suggestions for reducing this burden, to Department of Defense, Washington Headquarters Services, Directorate for Information Operations and Reports (0704-0188), 1215 Jefferson Davis Highway, Suite 1204, Arlington, VA 22202-4302. Respondents should be aware that notwithstanding any other provision of law, no person shall be subject to any penalty for failing to comply with a collection of information if it does not display a currently valid OMB control number. PLEASE DO NOT RETURN YOUR FORM TO THE ABOVE ADDRESS.</p>				
1. REPORT DATE (DD-MM-YY)		2. REPORT TYPE		3. DATES COVERED (From - To)
22 September 2017		Interim		1 August 2014 – 22 August 2017
4. TITLE AND SUBTITLE		<p>CASE STUDY OF MODEL-BASED INVERSION OF THE ANGLE-BEAM ULTRASONIC RESPONSE FROM COMPOSITE IMPACT DAMAGE (POSTPRINT)</p>		
6. AUTHOR(S)		<p>1) Laura Homa – UDRI</p> <p>2) John Wertz, John Welter, and Daniel Sparkman – AFRL/RX</p> <p>(Continued on page 2)</p>		
7. PERFORMING ORGANIZATION NAME(S) AND ADDRESS(ES)		<p>1) University of Dayton Research Institute 300 College Park Dayton, OH 45469</p> <p>2) AFRL/RX Wright-Patterson Air Force Base Dayton, OH 45433</p> <p>(Continued on page 2)</p>		
9. SPONSORING/MONITORING AGENCY NAME(S) AND ADDRESS(ES)		<p>Air Force Research Laboratory Materials and Manufacturing Directorate Wright-Patterson Air Force Base, OH 45433-7750</p> <p>Air Force Materiel Command United States Air Force</p>		
12. DISTRIBUTION/AVAILABILITY STATEMENT		Distribution Statement A. Approved for public release: distribution unlimited.		
<p>13. SUPPLEMENTARY NOTES</p> <p>PA Case Number: 88ABW-2016-4670; Clearance Date: 22 Sep 2017. This document contains color. Journal article published in Journal of Nondestructive Evaluation, Diagnostics, Vol. 1, 5 Jun 2018. © 2018 ASME. The U.S. Government is joint author of the work and has the right to use, modify, reproduce, release, perform, display, or disclose the work.</p> <p>The final publication is available at http://nondestructive.asmedigitalcollection.asme.org DOI: 10.1115/1.4040233</p>				
<p>14. ABSTRACT (Maximum 200 words)</p> <p>The U.S. Air Force seeks to improve lifecycle management of composite structures. Nondestructive characterization of damage is a key input to this framework. One approach to characterization is model-based inversion of ultrasound inspection data; however, the computational expense of simulating the response from damage represents a major hurdle for practicality. A surrogate forward model with greater computational efficiency and sufficient accuracy is, therefore, critical to enable damage characterization via modelbased inversion. In this work, a surrogate model based on Gaussian process regression (GPR) is developed on the chirplet decomposition of the simulated quasi-shear scatter from delamination-like features that form a shadowed region within a representative composite layup. The surrogate model is called in the solution of the inverse problem for the position of the hidden delamination, which is achieved with <0.5% error in <20 min on a workstation computer for two unique test cases. These results demonstrate that solving the inverse problem from the ultrasonic response is tractable for composite impact damage with hidden delaminations.</p>				
<p>15. SUBJECT TERMS</p> <p>Shear wave ultrasound; composite impact damage; model-based inversion; delamination; Gaussian process; chirplet</p>				
16. SECURITY CLASSIFICATION OF:		17. LIMITATION OF ABSTRACT:	18. NUMBER OF PAGES	19a. NAME OF RESPONSIBLE PERSON (Monitor)
a. REPORT Unclassified	b. ABSTRACT Unclassified	c. THIS PAGE Unclassified	SAR 13	John Wertz 19b. TELEPHONE NUMBER (Include Area Code) (937) 255-2718

REPORT DOCUMENTATION PAGE Cont'd

6. AUTHOR(S)

- 3) John Aldrin – Computational Tools

7. PERFORMING ORGANIZATION NAME(S) AND ADDRESS(ES)

- 2) Computational Tools
4275 Chatham Ave, Gurnee, IL 60031

John Wertz¹

Air Force Research Laboratory,
2977 Hobson Way,
Wright-Patterson AFB, OH 45433
e-mail: john.wertz.1@us.af.mil

Laura Homa

Structural Materials Division,
University of Dayton Research Institute,
300 College Park,
Dayton, OH 45469

John Welter

Air Force Research Laboratory,
2977 Hobson Way,
Wright-Patterson AFB, OH 45433

Daniel Sparkman

Air Force Research Laboratory,
2977 Hobson Way,
Wright-Patterson AFB, OH 45433

John C. Aldrin

Computational Tools,
Gurnee, IL 60031

Case Study of Model-Based Inversion of the Angle Beam Ultrasonic Response From Composite Impact Damage

The U.S. Air Force seeks to improve lifecycle management of composite structures. Non-destructive characterization of damage is a key input to this framework. One approach to characterization is model-based inversion of ultrasound inspection data; however, the computational expense of simulating the response from damage represents a major hurdle for practicality. A surrogate forward model with greater computational efficiency and sufficient accuracy is, therefore, critical to enable damage characterization via model-based inversion. In this work, a surrogate model based on Gaussian process regression (GPR) is developed on the chirplet decomposition of the simulated quasi-shear scatter from delamination-like features that form a shadowed region within a representative composite layup. The surrogate model is called in the solution of the inverse problem for the position of the hidden delamination, which is achieved with <0.5% error in <20 min on a workstation computer for two unique test cases. These results demonstrate that solving the inverse problem from the ultrasonic response is tractable for composite impact damage with hidden delaminations. [DOI: 10.1115/1.4040233]

1 Introduction

The increasing use of polymer–matrix composites within Air Force structures has fueled a growing demand for improved lifecycle management of these materials [1]. The Air Force Aircraft Structural Integrity Program guidelines for metallics provide the template for this improvement, where validated damage progression models enable tolerance to assumed defects for an acceptable measure of risk [2]. Composites damage progression models are sensitive to the geometric complexity of typical damage modes. Consequently, nondestructive evaluation (NDE) techniques are needed to volumetrically represent damage for improved lifecycle management.

Currently viable composite NDE methods include X-ray–computed tomography (XCT) and ultrasound. XCT scans volumetrically reconstruct internal damage, making it an obvious path for feature characterization. Nevertheless, XCT cannot be used in situ as a single-sided inspection and generally requires additional safety precautions. By contrast, normal incidence longitudinal wave ultrasound can detect the presence of delaminations and matrix cracking in a single-sided inspection (Fig. 1(a)). However, it is incapable of insonifying the hidden damaged region under the top delamination layers (Fig. 1(b)). A novel angle beam shear wave method addresses this limitation by using direct and back-wall reflected quasi-shear waves to inspect for hidden ply delaminations and matrix cracks [3,4]. This approach builds on prior work on polar backscatter ultrasonic techniques [5–8]. In this way, additional information from hidden damage features can be captured and processed to characterize the damage producing the observed response. It should be noted that phased array transducers (either in a normal incidence or angle beam shear configuration) may provide additional information; however, for the purposes of this work, the simplest sensing approach (single

element, pulse-echo inspection) was selected based on the complexity of the material and internal damage.

One challenge with this angle beam ultrasonic inspection technique is resolving the multiple signals scattered from delamination edges at different depths. Manual interpretation of the paths for each signal is complicated, as the scattered signals interact with the composite panel surfaces and neighboring delaminations. Model-based inversion is proposed to address this challenge. This approach uses nonlinear least-squares based optimization to estimate the parameters of a physics-based forward model by minimizing an objective function defined as the squared residual between the model output and the observed response. Prior work has considered flaw reconstructions with ultrasonic NDE in anisotropic materials [9–13]. Other efforts have examined the use of multipath signals for characterizing the location of scatterers [14–17]. For example, Hutt and Simonetti used a strongly scattering planar interface as a mirror to look behind the object to achieve complete reconstruction [17]. Some studies have investigated the identification of multiply diffracted ultrasonic waves from point scatterers, although many of them have focused on medical ultrasound applications [18,19]. Most approaches outlined within the literature have leveraged approximate models like ray theory for improving reconstruction. The proposed solution builds on prior work using numerical solutions of parameterized models to invert the damage state [20–22]. The specific problem of inverting the location of multiple impact damage discontinuities in a thin composite panel has not been addressed to date. In this work, a simplified case study was investigated to demonstrate the model-based inversion approach.

2 Materials and Methods

The geometry of impact damage within a composite is dependent on the size, shape, and velocity of the impactor; the interaction of the deforming impactor with the shape and orientation of the structure; and the current mechanical state of the material as a function of as-manufactured properties, internal defects, thermomechanical degradation, and environment. These variables result

¹Corresponding author.

Manuscript received October 27, 2017; final manuscript received May 7, 2018; published online June 5, 2018. Assoc. Editor: Paul Fromme.

This work is in part a work of the U.S. Government. ASME disclaims all interest in the U.S. Government's contributions.

in asymmetric, highly irregular damage contours. Bench-top impact tests on laboratory coupons can control some of these variables, albeit with little reduction in the geometric complexity of the damage.

A simple representative problem, estimation of the location of a hidden delamination beneath a top delamination, was considered to reduce geometric complexity to a level suitable for a feasibility study. Two cases are presented in Fig. 2: in case 1, the lower (hidden) delamination was fixed in z with the x -position iterated through nine values; in case 2, the lower delamination was fixed in x with the z -position iterated through eight values.

The parameters for the study follow existing specimens and laboratory testing conditions [23]. A 3.2 mm thick, 24 ply IM7/977-3 composite panel of $[-45\text{ deg}/90\text{ deg}/45\text{ deg}/0\text{ deg}]_s$ layup with simplified delamination-like features was considered. The simulated ultrasonic transducer was 6.35 mm in diameter, with a center frequency of 5 MHz and a focal length of 19.05 mm. The angle of incidence was set to 24 deg, near the first critical angle of the homogenized composite (~ 27 deg) such that the incident beam was refracted into quasi-shear modes at the front-wall. The simulated delaminations were each 12.7 mm long. Their locations did not directly coincide with ply interfaces but did not exceed a minimum of a single ply separation in the z -direction. These cases provide an elegant demonstration of the proposed method of solving the inverse problem while leaving room for follow-on studies

addressing the challenges of a much larger set of pertinent parameters.

3 Calculation

3.1 Forward Model and Need for Surrogate Representation. The efficiency of model-based inversion is proportional to the well-posedness of the problem and inversely proportional to the cost of each forward model iterate. Two computational tools—CIVA FIDEL 2D and PZFlex—are tailored for ultrasound simulation of composite materials [24–26]. CIVA FIDEL 2D couples semi-analytical beam calculations with a finite difference time domain (FDTD) solver acting on a user-specified region to model two-dimensional (2D) wave propagation for simple geometries and boundary conditions [27,28]. Comparatively, PZFlex uses finite element analysis with an optimized explicit solver to simulate 2D or three-dimensional wave propagation on any geometry with complex boundary conditions. Both tools can simulate a spatially dense B-scan response from thin delamination-like features in a representative composite material within several hours; however, typical inverse problems often require hundreds of model calls. For a 2D ultrasonic inspection scenario, solution times would range from days to weeks. When the physics-based model is computationally expensive, a surrogate will often be developed that sacrifices some accuracy for a decrease in

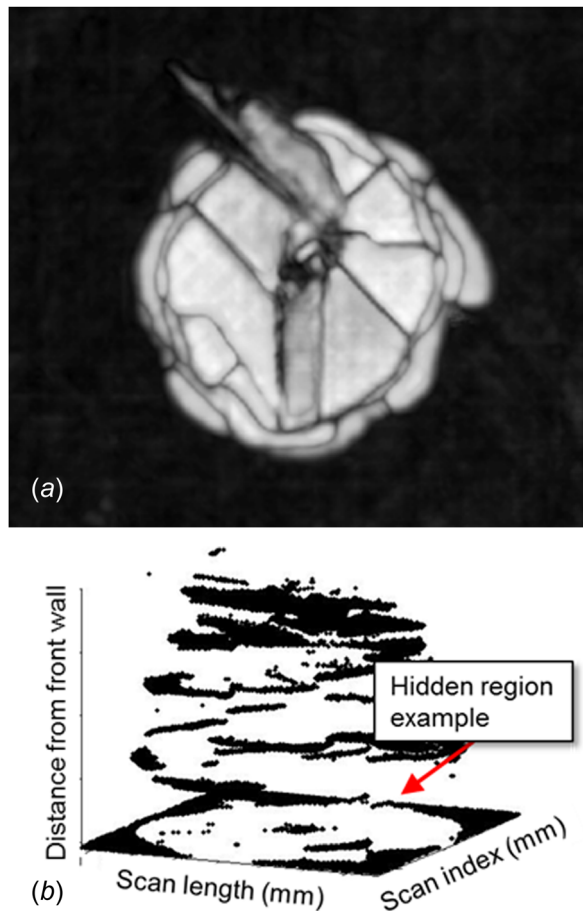


Fig. 1 Impact delamination in a composite coupon. Amplitude and time-of-flight data describes the complexity of composite impact damage and hidden delamination regions invisible to a normal incidence longitudinal wave single-sided inspection: (a) normal incidence C-Scan of impact damage with visible petal-shaped delaminations based on amplitude data and (b) representation of a hidden region (white) in a delamination field (black) based on time-of-flight data.

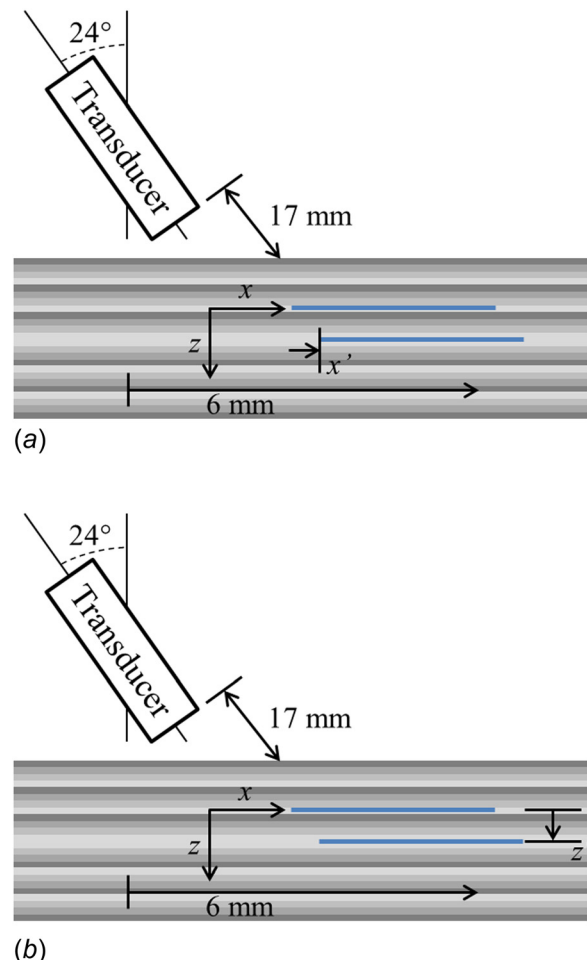


Fig. 2 Schematics of surrogate model demonstration cases 1 (a) and 2 (b). The transducer is 6.35 mm in diameter, with a center frequency of 5 MHz and a 19.05 mm focal length. Delamination features are 12.7 mm long. The diagrammed scan path is not to scale: (a) hidden delamination varying in x -direction, fixed z at $z = 2$ mm and (b) hidden delamination varying in z -direction, fixed x at $x = 1.2$ mm.

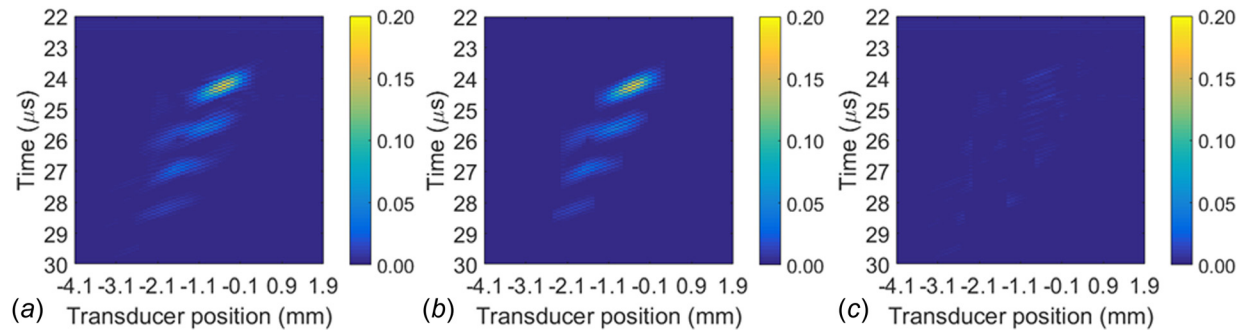


Fig. 3 Chirplet representation of an example B-scan. (a) The original B-scan from CIVA. (b) The chirplet reconstruction of the B-scan. (c) The residual between the original B-scan and the reconstruction. The color bar represents the amplitude of the response in (a) and (b) and the amplitude of the residual in (c) [34].

computational expense [29]. The need for an efficient surrogate model is evident for the ultrasound inverse problem; thus, CIVA was chosen for surrogate model development based on its greater computational efficiency, the dimensionality of the scenario, and previous validation work [4].

Previous work demonstrated the feasibility of an ultrasound surrogate model for the case of a single delamination placed in four unique z -positions [30]. In this work, a similar model is developed on the more challenging case of a hidden delamination. Model development began with selection of the representative

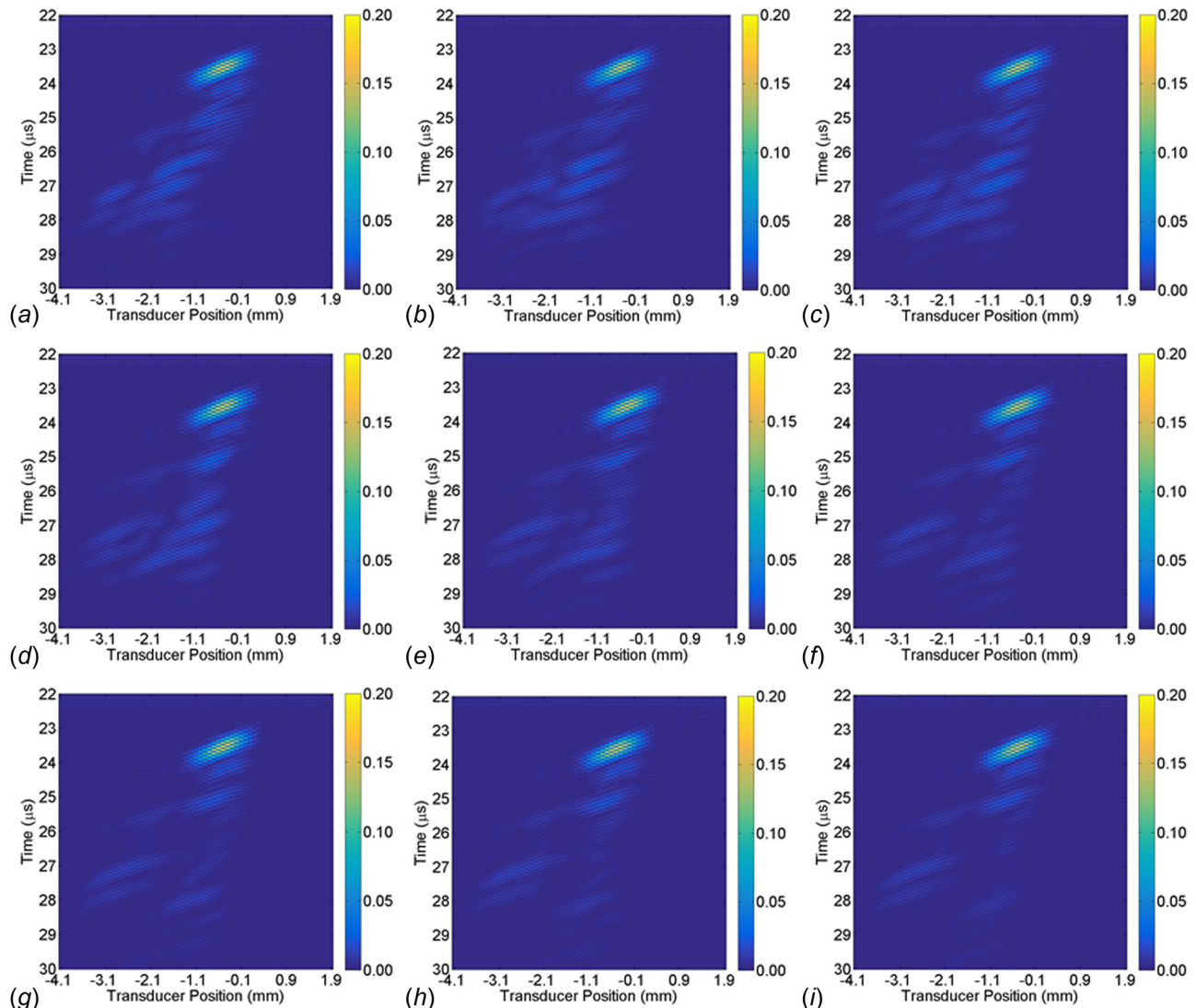


Fig. 4 Hidden delamination simulations for nine hidden delamination x -positions. The x -position range was selected to ensure that the delamination was hidden but not so far from the tip of the topmost delamination that indications from the hidden delamination were no longer visible. The color bar describes the amplitude of the response: (a) $x = 0.8$ mm, (b) $x = 1.0$ mm, (c) $x = 1.2$ mm, (d) $x = 1.4$ mm, (e) $x = 1.6$ mm, (f) $x = 1.8$ mm, (g) $x = 2.0$ mm, (h) $x = 2.2$ mm, and (i) $x = 2.4$ mm.

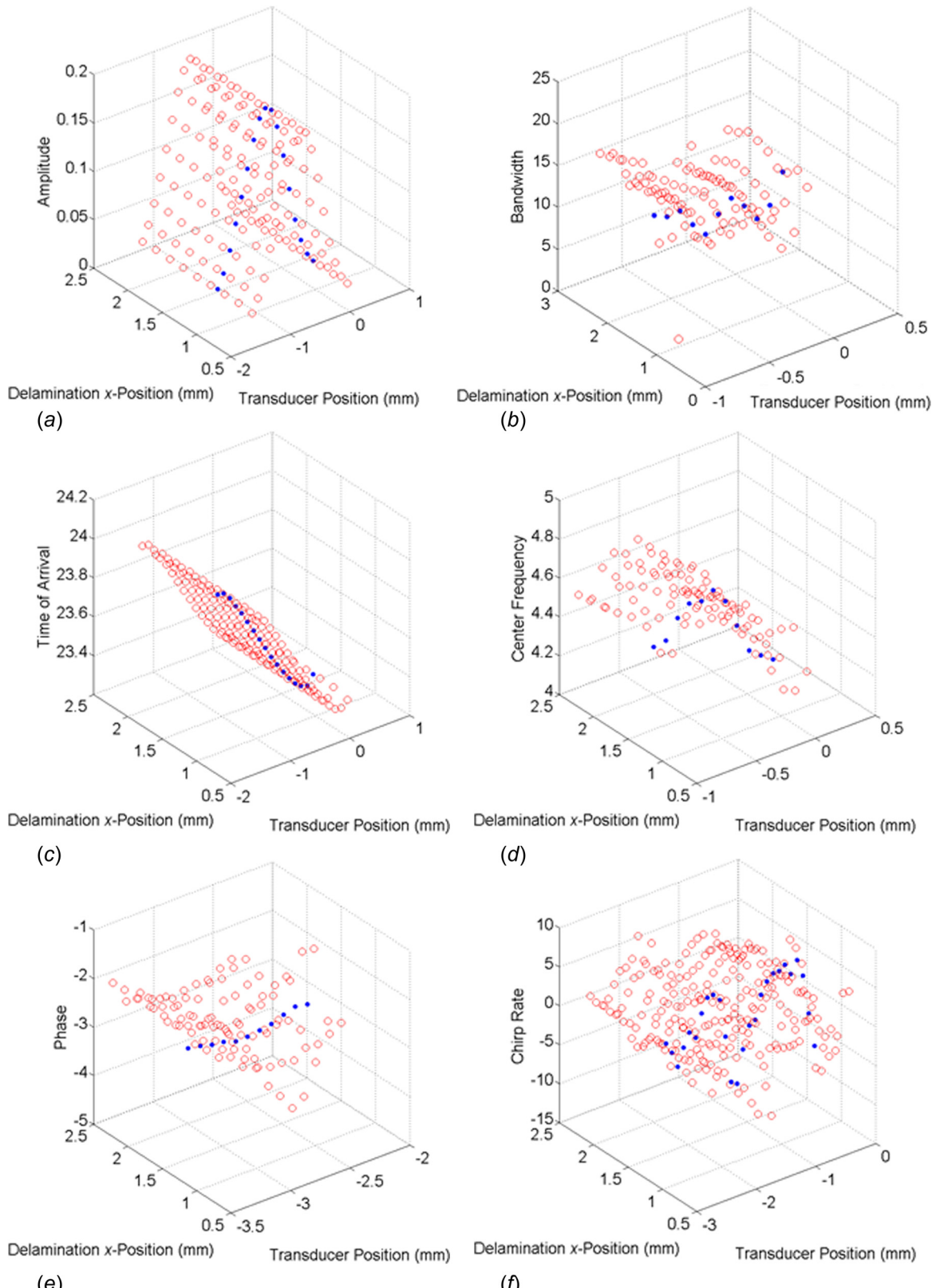


Fig. 5 Gaussian chirplet parameters and GPR estimates for case 1. Open circles are parameters from CIVA and closed circles are parameter estimates. (a) and (c) vary smoothly, while (e) and (f) exhibit strong variation. (a) Reflection 1 amplitude, (b) reflection 2 bandwidth, (c) reflection 1 time of arrival, (d) reflection 2 center frequency, (e) reflection 8 phase, and (f) reflection 3 chirp rate.

problem, which was modeled in CIVA FIDEL 2D for a sparse set of design points containing the inverse solution. Chirplet decomposition was applied to each simulated B-scan; then, the surrogate model was constructed by interpolating on the chirplet parameter space via Gaussian process regression (GPR). The resulting fits formed the surrogate model used to solve the inverse problem for the ultrasonic response from a hidden delamination with an unknown x - or z -position.

3.2 B-Scan Simulation. Several assumptions were made for the simulation. First, it was assumed that the composite was flat and parallel, which is valid for a simulation-based study but likely invalid for real composite panels. Second, it was assumed that delaminations could be modeled as discontinuities with zero thickness parallel to the plies. While acceptable for a simulation-based study, real delamination morphologies should be incorporated to validate this assumption. Finally, it was assumed that water is present on the backside of the composite. This assumption would hold true for a real panel scanned via immersion ultrasound; however, an air back-wall is more likely for real inspection scenarios.

The model consisted of a water path to simulate an immersion-based inspection, the plies forming the composite panel, and delamination features. Because of the FIDEL package, the plies were modeled individually (the composite was not homogenized). For these boundary conditions, a 2D FDTD region was set to surround the near edges of the delaminations and the composite panel boundaries. The FDTD solution region moves with the scanned probe, so the lateral extent was set to a large size (20 mm) in order to include both direct and full skip interactions with the far-wall. Perfectly matched layers were also applied to the lateral boundaries to help control fictitious signals from the model domain edges. A mesh resolution was fixed to 1/20th of the center frequency wavelength. Additional details of the formulation can be found in published literature [27,28]. B-scan images were

generated by scanning the transducer over a 6 mm path across the top of the composite in 0.1 mm increments with a constant water path of 17 mm. Simulations were performed on a HP computer with two 12-core hyperthreaded processors (48 compute cores) at 2.5 GHz clock speed and 98 GB of RAM. Each B-scan required \sim 360 min of simulation time. An example simulated B-scan for a single delamination located at 1.0 mm in depth from the top surface is shown in Fig. 3(a). In this case, the largest signal is a direct diffraction from the delamination edge. Signals later in time correspond to the multiple paths for diffracted responses interacting with the top or bottom surfaces of the composite. Half-skips involve a single reflection off of the back-wall surface, while full-skips involve two reflections off of the back-wall. These signals shift in time and space according to the position of the delamination edge.

3.3 Chirplet Decomposition. It is nontrivial to produce B-scans via the physics-based forward model given the nature of the shifting transient signals with varying delamination position and the size of the simulated B-scans results (61 scan steps \times 1350 time steps \sim 80k data points). To reduce the dimensionality of forward model results, individual A-scans were represented as a linear combination of Gaussian chirplets [31]. The Gaussian chirplet is defined as

$$f(t) = \beta \exp(-\alpha_1(t-\tau)^2) \cos(2\pi f_c(t-\tau) + \phi + \alpha_2(t-\tau)^2) \quad (1)$$

where β is the amplitude of the Gaussian envelope, α_1 is the bandwidth of the Gaussian envelope, τ is the time of arrival of the response, f_c is the center frequency, ϕ is the phase angle, and α_2 is the chirp rate. The chirp rate, α_2 , captures the variation of frequency with respect to time and represents a substantial improvement over a wavelet-based approach. The chirplet has been shown

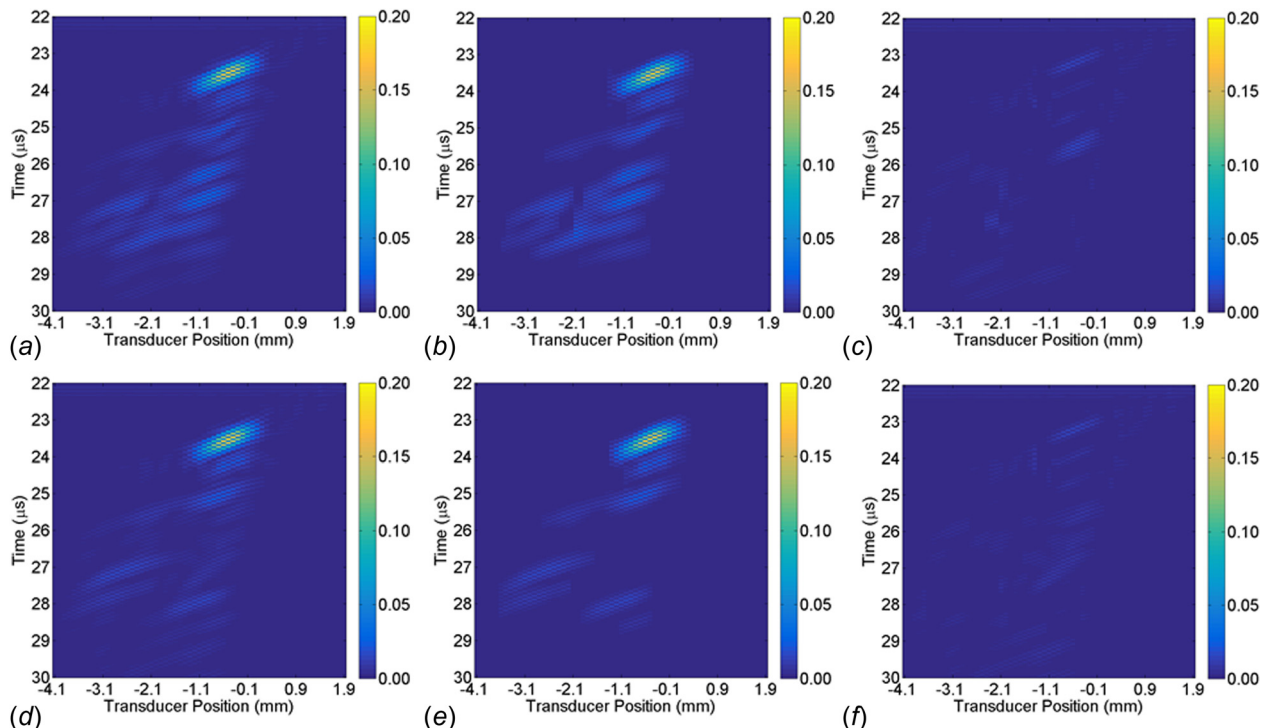


Fig. 6 Comparison of CIVA and surrogate model B-scans: (a)–(c) $x = 1.2$ mm and (d)–(f) $x = 2.0$ mm. (a) and (d) depict the original CIVA B-scan, (b) and (e) depict the chirplet reconstruction of the B-scan, and (c) and (f) depict the residual between the CIVA B-scan and the chirplet reconstruction. The residual is a mixture of untracked reflections and incomplete chirplet fitting and is everywhere low. (a) CIVA B-scan, $x = 1.2$ mm, (b) chirplet reconstruction, $x = 1.2$ mm, (c) residual, $x = 1.2$ mm, (d) CIVA B-scan, $x = 2.0$ mm, (e) chirplet reconstruction, $x = 2.0$ mm, and (f) residual, $x = 2.0$ mm.

to model individual ultrasonic reflections as a sparse, energy preserving representation of the data without any a priori information on the expected response [31]. The chirplet parameters can be estimated from the analytic signal and further refined using a Gauss–Newton algorithm [32]. In the chirplet decomposition algorithm suggested in Refs. [31–33], chirplets are fit successively to individual A-scans until a reconstruction error tolerance is reached. The method used here differs slightly; rather than faithfully reconstructing each A-scan, chirplets only reproduced reflections in the B-scan that represented responses from a delamination. This was achieved by screening out reflections from the front-wall and back-wall of the composite—the remaining reflections were visually segmented and fitted. The surrogate model predicts how these individual reflections change with the position of the hidden delamination. Chirplet decomposition reduces the number of parameters needed to represent the B-scan to $6 \sum_{j=1}^N n_j$, where N is the total number of distinct reflections, and n_j is the number of transducer positions containing a signal from the j th reflection. As an example, Fig. 3 depicts a B-scan containing ~ 80 k samples, while the chirplet reconstruction is defined by ~ 360 chirplet parameters [34].

3.4 Gaussian Process Regression. Techniques such as splining, support vector machines, and GPR were considered for use as a surrogate for the physics-based forward model. Gaussian process regression, also known as kriging, was chosen as the metamodel for its efficiency, robustness, and flexibility, and has a history of use as a metamodel [35–37]. A type of supervised

learning, GPR generates input–output mappings from the training data. The estimation of the function value f at a test point u is described by

$$f(u) = \mu(u) + c_u^T (C + \sigma_n^2 I)^{-1} (y - \mu(s)) \quad (2)$$

The assumed mean function, μ , describes the general trend of the data. Both the covariance vector c_u between the test point(s) u and the sample points s and the covariance matrix C between the sample points s depend on the assumed covariance function. In the previous formulation, the known responses y recorded at the sample points s are assumed to be the sum of the unknown latent function values $f(s)$ and independent, identically distributed Gaussian noise with variance σ_n^2 . For this application, the inputs s are given by the transducer location and x - or z -position of the delamination, while the outputs y are the value of the chirplet parameter β , α_1 , τ , f_c , ϕ , or α_2 . For the case of simulation data, the variance σ_n^2 is assumed to be zero. The outputs f are the estimates of the chirplet parameters for the transducer locations at intermediate x - or z -positions of the hidden delamination.

Development of the GPR model begins with selection of the mean and covariance function. Both are assumed to be stationary. Example functions tested for fitting are presented for the mean (Eq. (3)) and covariance (Eq. (4))

$$\mu(u) = \left\{ a_o + a_1 u + L + a_n u^n \right\} \quad (3)$$

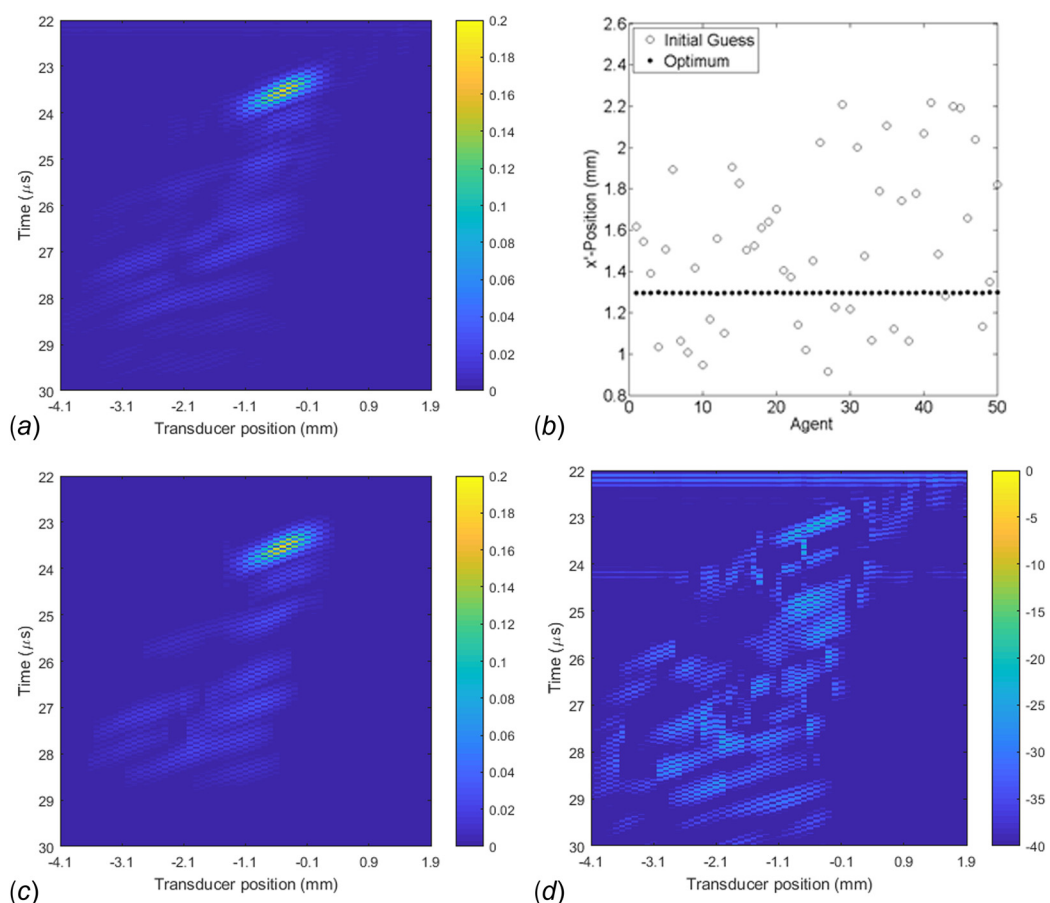


Fig. 7 CIVA B-scan (a), inverse solution (b), surrogate model evaluated at the inverse solution (c), and the residual in decibels (d). The inverse solution has an error of 0.22%, and the surrogate model at the inverse solution compares very well with the CIVA B-scan. (a) CIVA B-scan for $x = 1.3$ mm, (b) inverse solution for 50 initial guesses over 20 iterations, (c) surrogate model evaluated at $x = 1.297$ mm, and (d) residual in decibels.

$$k(s_i, s_j) = \begin{cases} \exp(-\|s_i - s_j\|_2/l) \\ \exp(-\|s_i - s_j\|_2^2/2l^2) \end{cases} \quad (4)$$

In Eq. (3), u are the test point(s), c is a constant, a_i are polynomial coefficients, and n is the order of the term. In Eq. (4), s are the sample points and $\|\cdot\|_2$ denotes the Euclidean distance. The parameter l describes how rapidly the correlation between samples decreases and is a hyperparameter of the GPR model optimized via leave-one-out cross validation on the input data; thus, the value of l varies between parameters and reflections [38]. Selection of the mean and covariance functions is often guided by physics-based expectations of the response; however, mathematically rigorous model selection techniques such as the Akaike information criterion (AIC, Eq. (5)) can be applied

$$\text{AIC} = -(2/N)E[\log \text{lik}] + (2d/N) \quad (5)$$

The AIC rewards model accuracy (the first term, where N is the number of samples) while penalizing complexity (the second term, where d is the number of model parameters), with better

models producing more highly negative values [39]. For this work, the response from each parameter was fit with every combination of the selected mean and covariance functions, with the combination producing the lowest AIC selected as the optimal set for that parameter. The surrogate model results from the best performing mean and covariance function combination with an optimized hyperparameter l . An input vector u is developed for each intermediate x - or z -position of the hidden delamination and applied to the GPR model. The output of the model is the estimate of the selected parameter for a given reflection.

4 Results and Discussion

4.1 Case 1: x -Varying, z -Fixed. For this demonstration, the z -position of the lower delamination was fixed at 2 mm from the upper delamination, while x ranged from 0.8 mm to 2.4 mm in nine steps from the leftmost edge of the upper delamination. This range was selected due to the evident variations in reflection position and intensity at each delamination position. Changes between B-scans diminish drastically beyond $x = 2.4$ mm, resulting in regions where unique solutions to the inverse problem

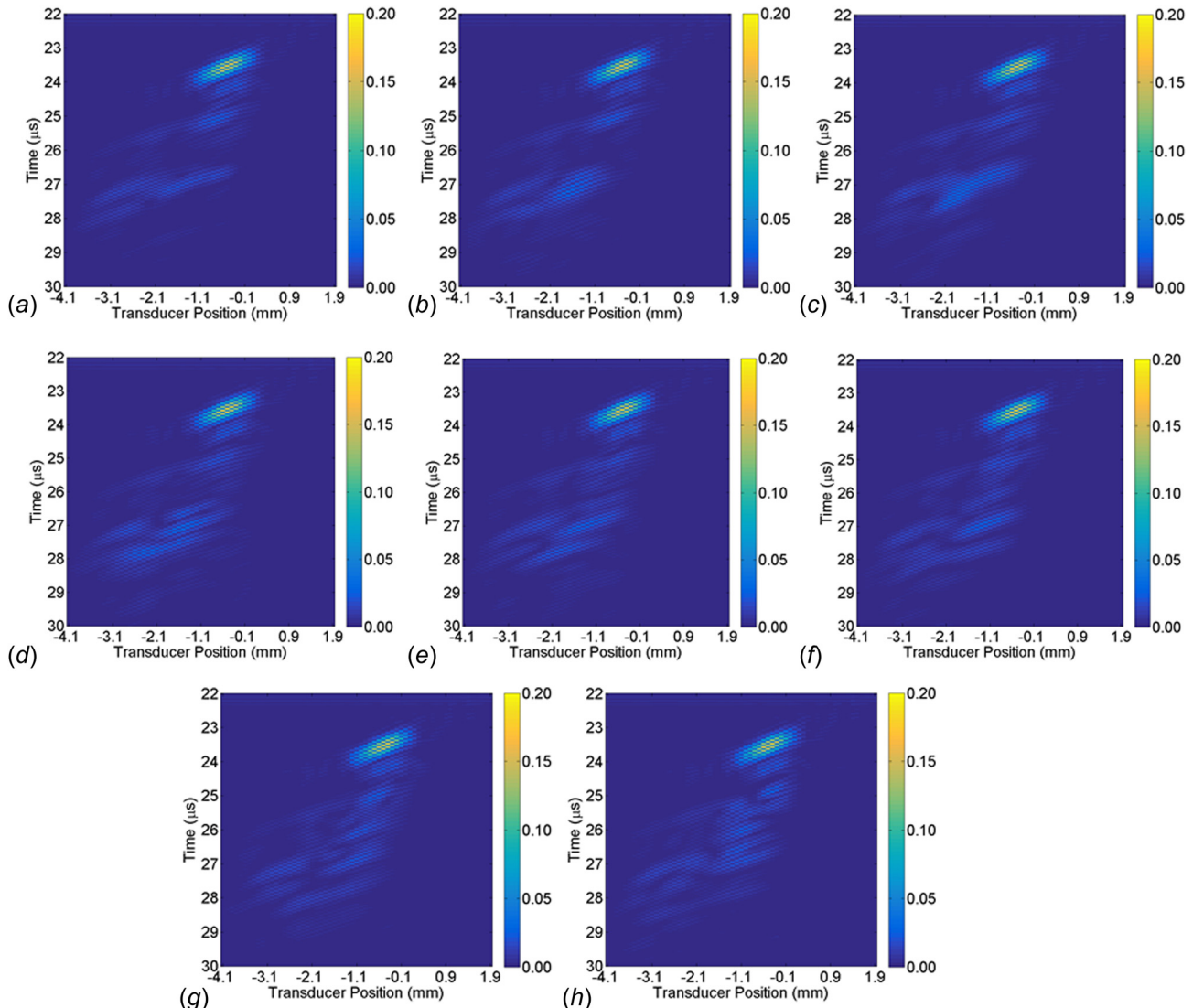


Fig. 8 Hidden delamination simulations for eight second-delamination z -positions. The z -position range was selected to ensure that the second delamination was hidden but not so close to the topmost delamination that the reflections fully merge and become indistinguishable. The color bar describes the amplitude of the response: (a) $z = 1.1$ mm, (b) $z = 1.3$ mm, (c) $z = 1.5$ mm, (d) $z = 1.7$ mm, (e) $z = 1.9$ mm, (f) $z = 2.1$ mm, (g) $z = 2.3$ mm, and (h) $z = 2.5$ mm.

hypothetically do not exist. The temporospatial translations of nine reflections were tracked across each B-scan. These reflections were selected in order of decreasing amplitude, with the bounds of each reflection governed by the envelope of the chirplet in the time dimension and the threshold for fitting a chirplet to an observed signal in the spatial direction. The B-scans used for building the surrogate model are presented in Fig. 4. Tracked reflections generally maintain their original shape as the hidden delamination varies from $x = 0.8$ mm to $x = 1.4$ mm, although the strength of the response from later reflections begins to diminish. From $x = 1.4$ to $x = 2.0$ more reflections appear, while those later in time continue to decrease in amplitude. Finally, later reflections diminish to the point where their amplitude is below the threshold for chirplet fitting between $x = 2.0$ and $x = 2.4$.

Sample data were drawn from Gaussian chirplet parameters for a given delamination x -position. Three mean basis functions (constant, linear, and quadratic) (Eq. (3)) and two covariance basis functions (Eq. (4)) were competed for each parameter fit using the AIC. In general, the Gaussian covariance function provided the most accurate representation of the observed data. The optimal mean function varied from parameter to parameter, although less sensitivity to the mean function was observed. To demonstrate the surrogate model for case 1, selected Gaussian chirplet parameters and the GPR model fits from the nine reflections for $x = 1.3$ mm are presented in Fig. 5. Several of the parameters vary smoothly across a given reflection (e.g., amplitude and time of arrival, Figs. 5(a) and 5(c), respectively), although few parameters are uniformly smooth across all reflections (e.g., reflection eight phase and reflection three chirp rate, Figs. 5(e) and 5(f), respectively). As the quality of the chirplet representation is most sensitive to the amplitude and time of arrival of the signal, the smoothness of the response from these parameters is highly encouraging for accurate representation of an intermediate B-scan location.

Fitted parameters were used to reconstruct the B-scan for test positions of $x = 1.2$ mm and $x = 2.0$ mm as presented in Figs.

6(a)–6(c) and 6(d)–6(f), respectively. The quality of the surrogate was judged by the residual between the simulated B-scan for that delamination location and the estimated B-scan. Construction of the B-scan from the surrogate model took 52 ms. As the nine tracked reflections were selected based in order of decreasing amplitude, the residual for both cases is dominated by low-amplitude reflections; however, some response from tracked reflections (most notably the residual arising from the first, largest reflection) was not fully modeled by the chirplet fits.

The true performance of the surrogate model is measured by its ability to rapidly and accurately invert a B-scan with a delamination in an unknown position. This was tested by first simulating a CIVA B-scan for an intermediate point in the surrogate model (lower delamination positioned at $x = 1.3$ mm). Next, an optimization algorithm was applied to minimize the residual sum-of-squares between the supplied B-scan and that generated by the surrogate model. As reflections may appear or disappear as the x -position of the hidden delamination is changed, an algorithm that handles discontinuities in the search space was required. The differential evolution (DE) algorithm was, thus, selected [40].

The CIVA B-scan, initial guesses and final solution of the DE algorithm, surrogate model evaluated at the final solution, and the residual in decibels are presented in Figs. 7(a)–7(d), respectively.

Twenty iterations of the DE algorithm were evaluated using 50 initial points covering the possible solution space, resulting in a final solution of $x = 1.297$ mm. This result has an error of 0.22% with a runtime of ~ 18 min on a standard workstation. Visually, the B-scan reconstructed for $x = 1.297$ mm appears nearly indistinguishable from the CIVA B-scan at $x = 1.3$ mm, further demonstrating the quality of the inversion.

4.2 Case 2: z -Varying, x -Fixed. For case 2, the x -position of the lower delamination was fixed at 1.2 mm from the leftmost edge of the upper delamination, while z ranged from 1.1 mm to

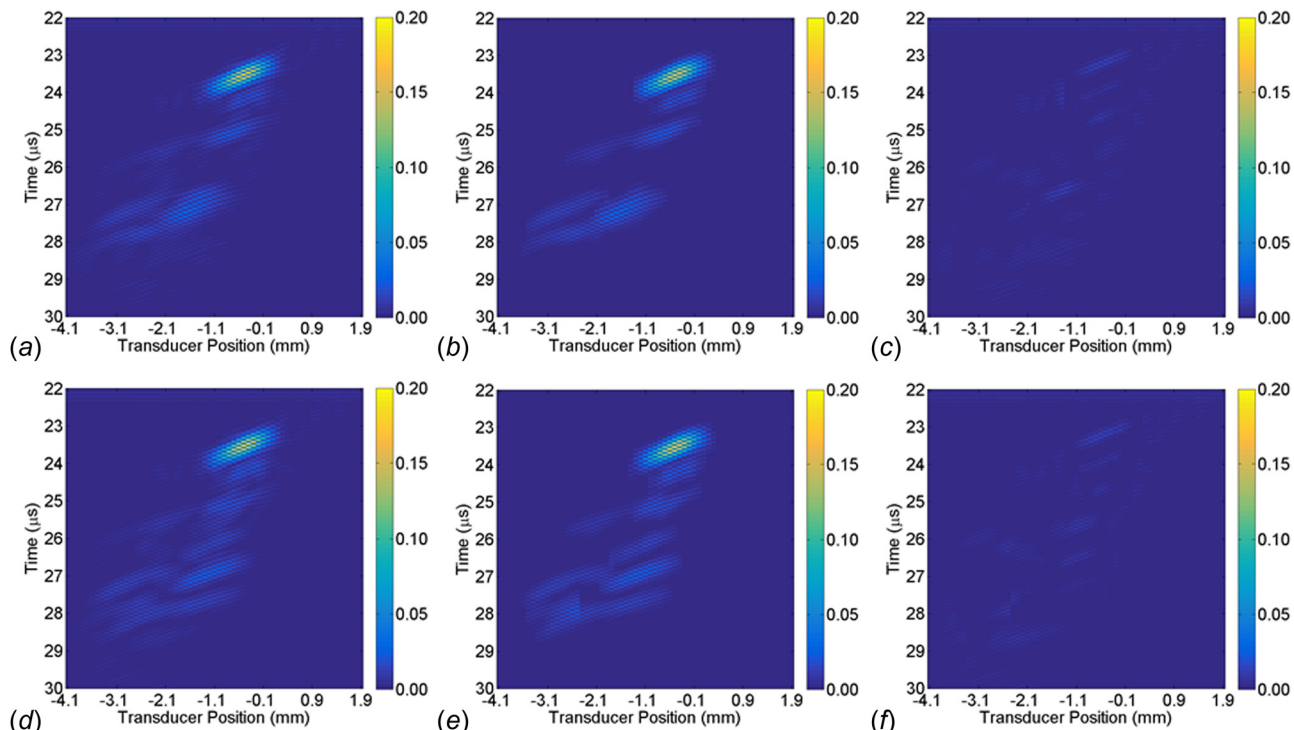


Fig. 9 Comparison of CIVA and surrogate model B-scans, (a)–(c) $z = 1.3$ mm and (d)–(f) $z = 2.1$ mm. (a) and (d) depict the original CIVA B-scan, (b) and (e) depict the chirplet reconstruction of the B-scan, and (c) and (f) depict the residual between the CIVA B-scan and the chirplet reconstruction. The residual is a mixture of untracked reflections and incomplete chirplet fitting and is everywhere low: (a) CIVA B-scan, $z = 1.3$ mm, (b) chirplet reconstruction, $z = 1.3$ mm, (c) residual, $z = 1.3$ mm, (d) CIVA B-scan, $z = 2.1$ mm, (e) chirplet reconstruction, $z = 2.1$ mm, and (f) residual, $z = 2.1$ mm.

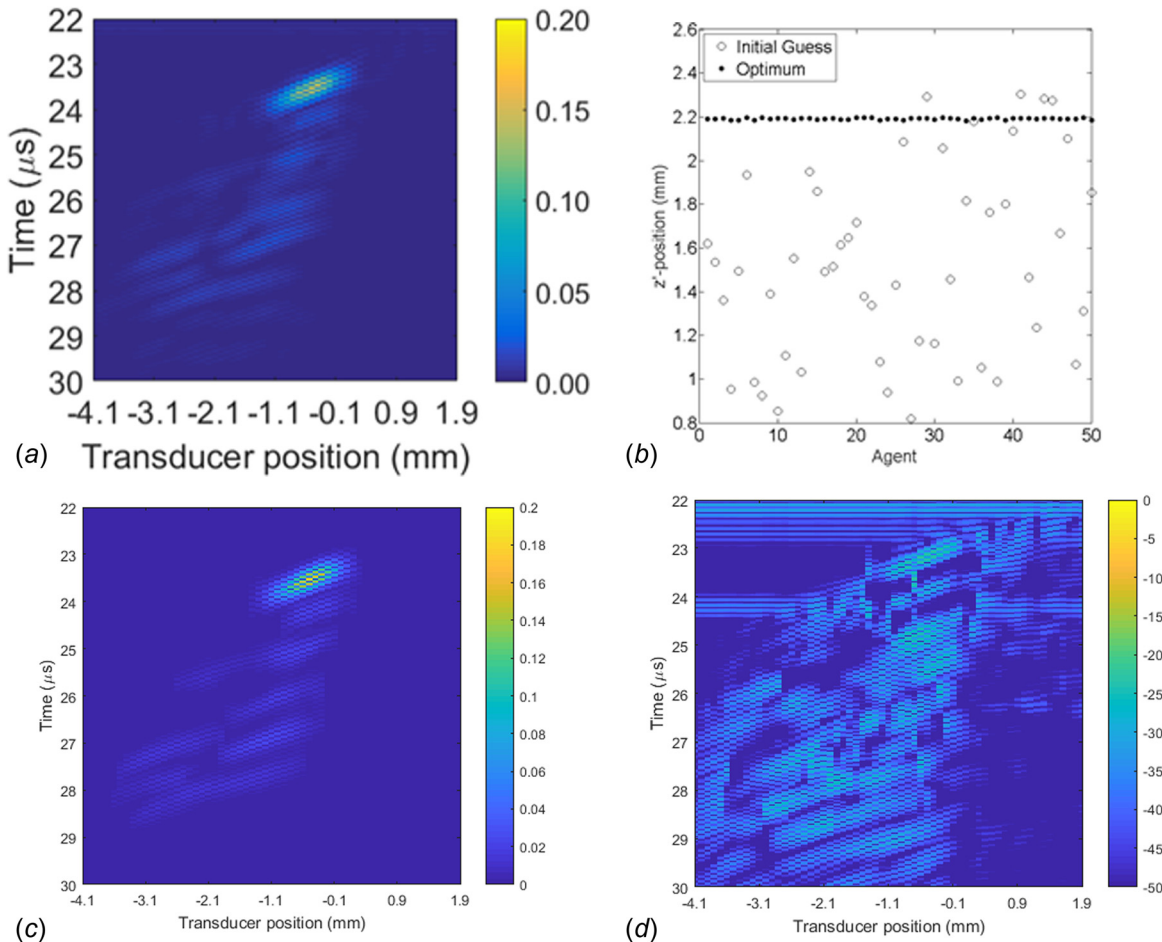


Fig. 10 CIVA B-scan (a), inverse solution (b), surrogate model evaluated at the inverse solution (c), and the residual in decibels (d). The inverse solution has an error of 0.41%, and the surrogate model at the inverse solution compares very well with the CIVA B-scan. (a) CIVA B-scan for $z = 2.2$ mm, (b) inverse solution for 50 initial guesses over 20 iterations, (c) surrogate model evaluated at $z = 2.191$ mm, and (d) residual in decibels.

2.5 mm from the upper delamination in eight steps. As before, the range of hidden delamination z -positions was chosen to ensure distinct variations in the intensity and position of the tracked reflections. The temporospatial translations of nine reflections were tracked across each B-scan. Reflections were selected in order of decreasing amplitude, with the bounds of each reflection governed by the envelope of the chirplet in the time dimension and the threshold for fitting a chirplet to an observed signal in the spatial direction. The B-scans developed for the surrogate model are presented in Fig. 8. As the hidden delamination moves from $z = 1.1$ mm to $z = 1.5$ mm, the reflections around $27 \mu\text{s}$ increase in size and complexity, although the general shape of the response remains mostly constant. Complex reflections beyond $25 \mu\text{s}$ appear and shift with the z -position of the hidden delamination from $z = 1.5$ mm to $z = 2.1$ mm.

Fitted parameters were used to reconstruct the B-scan for test positions of $z = 1.3$ mm and $z = 2.1$ mm as presented in Figs. 9(a)–9(c) and 9(d)–9(f), respectively. The quality of the surrogate was judged by the residual between the simulated B-scan for that delamination location and the estimated B-scan.

Construction of the B-scan from the surrogate model took 61 ms. As in case 1, the residual is dominated by low amplitude reflections or incomplete fitting of the primary reflection.

To test this case, a CIVA B-scan was generated for the lower delamination positioned at $z = 2.2$ mm. The CIVA B-scan, initial guesses and final solution of the DE algorithm, surrogate model evaluated at the inverse solution, and residual in decibels are presented in Figs. 10(a)–10(d), respectively. The DE algorithm was

again used with 20 iterations on 50 initial points covering the possible solution space. An inverse solution of $z = 2.191$ was found. This result has error of 0.41% with a runtime of ~ 14 min on a standard workstation. As observed in case 1, the B-scan reconstructed for $z = 2.191$ mm appears nearly indistinguishable from the CIVA B-scan at $z = 2.2$ mm, further demonstrating the quality of the inversion.

5 Conclusions

The ultrasonic response from a composite material with embedded delamination-like features was simulated for two test cases. Gaussian chirplets were fit to selected reflections within the simulated B-scans. Chirplet parameters and the position of the shifting coordinate (x or z) were used to develop GPR surrogate models. These models were used to estimate the unknown position of the hidden delamination for each test case. The unknown positions were rapidly estimated to within $< 0.5\%$ of the actual value, demonstrating that an efficient surrogate model can be developed on ultrasound simulations and that inversion of the ultrasonic response from delamination-like features is tractable for composite impact damage with hidden delaminations.

Practical application begins with an initial model of the material instantiated with the general shape of the delamination field based on a priori knowledge of relevant parameters (impact energy, layup, etc.). B-scans for permutations of this field would be generated, decomposed by the chirplet transform, and parameterized with Kriging to produce a surrogate model. The residual

between the parameterized model and the B-scan of the actual damage would be minimized, resulting in damage features matching those within the real composite structure.

Several challenges drive future work. First, chirplet decomposition relies on accurately mapping distinct reflections within the B-scan. While some degree of separation between responses is imposed by layup and ply thickness, the proximity of damage features often results in merged reflections. The current mapping approach requires user interpretation of the total response, which only compounds the challenge of selecting reflections to fit within the surrogate model. Algorithmic identification of individual reflections is, thus, crucial to enabling the inverse solution for complex damage morphologies. Second, the inverse problem was demonstrated for design points where reflections from the hidden delamination remain within the B-scan. These indications vanish as the hidden feature becomes further occluded by the upper delamination. Successive positions of the hidden delamination will eventually result in the same observed response, resulting in nonunique solutions to the inverse problem. Better methods of insonifying the hidden region is thereby critical to extending the range of tractable design cases. Third, experimental noise and variability from factors such as probe misalignment, water path, and transducer representation (e.g., dimensions/properties of the modeled piezoelectric crystal, backing material, or lens) are anticipated to impact the quality of the inverse solution. Parameter sensitivity studies will be employed to understand the impact of these sources of uncertainty. Finally, the techniques developed within this work could be extended to other relevant composite damage features, including fiber breakage and matrix cracking. Each feature type dominates failure for specific composite configurations, rendering them equally important in predicting the remaining loading cycles survivable by the damaged component.

Acknowledgment

The authors would like to acknowledge the support of Dr. Amanda Criner for guidance and technical support.

Funding Data

- Air Force Research Laboratory Materials and Manufacturing Directorate (Contract Nos. FA8650-14-D-5224 and FA8650-15-D-5231).

References

- [1] Mollenhauer, D., Iarve, E., Hoos, K., Flores, M., Zhou, E., Lindgren, E., and Schöppner, G., 2016, "Damage Tolerance for Life Management of Composite Structures—Part 1: Modeling," The Aircraft Structural Integrity Program Conference, ASIP Conference Proceedings, San Antonio, TX, Nov. 28–Dec. 1, pp. 3–5.
- [2] U.S. Department of Defense, 2005, "Department of Defense Standard Practice: Aircraft Structural Integrity Program (ASIP)," U.S. Department of Defense, VA, Standard No. **MIL-STD-1530C**.
- [3] Wertz, J., Wallentine, S., Welter, J., Dierken, J., and Aldrin, J., 2017, "Volumetric Characterization of Delamination Fields Via Angle Longitudinal Wave Ultrasound," *AIP Conf. Proc.*, **1806**, p. 090006.
- [4] Aldrin, J., Wertz, J., Welter, J., Wallentine, S., Lindgren, E., Kramb, V., and Zainey, D., 2018, "Review of Progress in Quantitative Nondestructive Evaluation," *AIP Conf. Proc.*, **1949**, p. 120005.
- [5] Johnston, P., Applegate, C., and Odarczenko, M., 2013, "Characterization of Delaminations and Transverse Matrix Cracks in Composite Laminates Using Multiple-Angle Ultrasonic Inspection," *AIP Conf. Proc.*, **1511**, pp. 1011–1018.
- [6] Bar-Cohen, Y., and Crane, R., 1982, "Acoustic-Backscattering Imaging of Subcritical Flaws in Composites," *Mater. Eval.*, **40**(9), pp. 970–975.
- [7] Raju, B., 1986, "Acoustic-Backscattering Studies of Transverse Cracks in Composite Thick Laminates," *Exp. Mech.*, **26**(1), pp. 71–78.
- [8] Gorman, M., 1991, "Ultrasonic Polar Backscatter Imaging of Transverse Matrix Cracks," *J. Compos. Mater.*, **25**(11), pp. 1499–1514.
- [9] Spies, M., and Jager, W., 2003, "Synthetic Aperture Focusing for Defect Reconstruction in Anisotropic Media," *Ultrasonics*, **41**(2), pp. 125–131.
- [10] Shlivinski, A., and Langenberg, K., 2007, "Defect Imaging With Elastic Waves in Inhomogeneous-Anisotropic Materials With Composite Geometries," *Ultrasonics*, **46**(1), pp. 89–104.
- [11] Li, C., Pain, D., Wilcox, P., and Drinkwater, B., 2013, "Imaging Composite Material Using Ultrasonic Arrays," *NDT E Int.*, **53**, pp. 8–17.
- [12] Lane, C., Dunhill, T., Drinkwater, B., and Wilcox, P., 2010, "3D Ultrasonic Inspection of Anisotropic Aerospace Components," *Insight*, **52**(2), pp. 72–77.
- [13] Fahim, A., Gallego, R., Bochud, N., and Rus, G., 2013, "Model-Based Damage Reconstruction in Composites From Ultrasound Transmission," *Compos. Part B*, **45**(1), pp. 50–62.
- [14] Lorenz, M., Van der Wal, F., and Berkhouit, A., 1993, "Optimization of Ultrasonic Defect Reconstruction With Multi-SAFT," *Rev. Prog. Quant. Nondestruct. Eval.*, **12**(A), pp. 851–858.
- [15] Lorenz, M., and Wielinga, T., 1993, "Ultrasonic Characterization of Defects in Steel Using Multi-SAFT Imaging and Neural Networks," *NDT E Int.*, **26**(3), pp. 127–133.
- [16] Ganansia, F., Chahbaz, A., and Mborokhi, K., 2000, "Experimental Evaluation of Weld Defects Using Multi-Path SAFT," *AIP Conf. Proc.*, **509**, p. 1341.
- [17] Hutt, T., and Simonetti, F., 2010, "Reconstructing the Shape of an Object From Its Mirror Image," *J. Appl. Phys.*, **108**(6), p. 064909.
- [18] Löer, K., Meles, G., and Curtis, A., 2015, "Automatic Identification of Multiply Diffracted Waves and Their Ordered Scattering Paths," *J. Acoust. Soc. Am.*, **137**(4), pp. 1834–1845.
- [19] Labyed, Y., and Huang, L., 2014, "TR-MUSIC Inversion of the Density and Compressibility Contrasts of Point Scatterers," *IEEE Trans. Ultrason., Ferroelectr., Freq. Control*, **61**(1), pp. 16–24.
- [20] Tarantola, A., 2005, *Inverse Problem Theory*, Society for Industrial and Applied Mathematics, Philadelphia, PA.
- [21] Bonnet, M., and Constantinescu, A., 2005, "Inverse Problems in Elasticity," *Inverse Probl.*, **21**(2), p. R1.
- [22] Sabbagh, H., Murphy, R., Sabbagh, E., Aldrin, J., and Knopp, J., 2013, *Computational Electromagnetics and Model-Based Inversion—A Modern Paradigm for Eddy-Current Nondestructive Evaluation*, Springer, New York.
- [23] Welter, J., Wertz, J., Aldrin, J., Kramb, V., and Zainey, D., 2018, "Model-Driven Optimization of Oblique Angle Ultrasonic Inspection Parameters for Delamination Characterization," *AIP Conf. Proc.*, **1949**, p. 130005.
- [24] Deydier, S., Leymarie, N., Calmon, P., and Mengeling, V., 2006, "Modeling of the Ultrasonic Propagation Into Carbon-Fiber-Reinforced Epoxy Composites, Using a Ray Theory Based Homogenization Method," *AIP Conf. Proc.*, **820**, pp. 972–978.
- [25] Reverdy, F., Mahaut, S., Dominguez, N., and Dubois, P., 2015, "Simulation of Ultrasonic Inspection of Curved Composites Using a Hybrid Semi-Analytical/Numerical Code," *AIP Conf. Proc.*, **1650**, pp. 1047–1055.
- [26] Wojcik, G., Vaughan, D., Murray, V., and Mould, J., 1994, "Time-Domain Modeling of Composite Arrays for Underwater Imaging," *IEEE Ultrasonics Symposium*, Cannes, France, Oct. 31–Nov. 3, pp. 1027–1032.
- [27] Dominguez, N., and Reverdy, F., 2014, "Simulation of Ultrasonic Testing of Composite Structures," 11th European Conference on Non-Destructive Testing/ECNDT, Prague, Czech Republic, Oct. 6–10, http://www.ndt.net/events/ECNDT2014/app/content/Paper/344_Dominguez.pdf
- [28] Jezzine, K., Séguir, D., Ecault, R., Dominguez, N., and Calmon, P., 2017, "Hybrid Ray-FDTD Model for the Simulation of the Ultrasonic Inspection of CFRP Parts," *AIP Conf. Proc.*, **1806**, p. 090016.
- [29] Shell, E., Aldrin, J., Sabbagh, H., Sabbagh, E., Murphy, R., Mazdiyasni, S., and Lindgren, E., 2014, "Demonstration of Model-Based Inversion of Electromagnetic Signals for Crack Characterization," *AIP Conf. Proc.*, **1650**, pp. 484–493.
- [30] Wertz, J., Homa, L., Welter, J., Sparkman, D., and Aldrin, J., 2018, "Gaussian Process Regression of Chirplet Decomposed Ultrasonic B-Scans of a Simulated Design Case," *AIP Conf. Proc.*, **1949**, p. 130007.
- [31] Lu, Y., Demirli, R., Cardoso, G., and Saniie, J., 2006, "A Successive Parameter Estimation Algorithm for Chirplet Signal Decomposition," *IEEE Trans. Ultrason., Ferroelectr., Freq. Control*, **53**(11), pp. 2121–2131.
- [32] Demirli, R., and Saniie, J., 2014, "Asymmetric Gaussian Chirplet Model and Parameter Estimation for Generalized Echo Representation," *J. Franklin Inst.*, **351**(2), pp. 907–921.
- [33] Saniie, J., Lu, Y., and Demirli, R., 2006, "3E-3 A Comparative Study of Echo Estimation Techniques for Ultrasonic NDE Applications," *IEEE Ultrasonics Symposium*, Vancouver, BC, Oct. 2–6, pp. 436–439.
- [34] Homa, L., Wertz, J., Sparkman, D., Welter, J., and Aldrin, J., 2018, "Chirplet Decomposition for Surrogate Modeling of a Constrained Ultrasonic Design Case," *AIP Conf. Proc.*, **1949**, p. 130006.
- [35] Sparkman, D. M., Millwater, H. R., and Ghosh, S., 2013, "Probabilistic Sensitivity Analysis of Dwell-Fatigue Crack Initiation Life for a Two-Grain Microstructural Model," *Fatigue Fract. Eng. Mater. Struct.*, **36**(10), pp. 994–1008.
- [36] Santner, T. J., Williams, B. J., and Notz, W., 2003, *The Design and Analysis of Computer Experiments. Springer Series in Statistics*, Springer-Verlag Inc., New York.
- [37] Martin, J. D., and Simpson, T. W., 2005, "Use of Kriging Models to Approximate Deterministic Computer Models," *AIAA J.*, **43**(4), pp. 853–863.
- [38] Rasmussen, C., and Williams, C., 2006, *Gaussian Processes for Machine Learning*, Vol. 1, MIT Press, Cambridge, MA.
- [39] Friedman, J., Hastie, T., and Tibshirani, R., 2001, *The Elements of Statistical Learning*, Vol. 1, Springer Series in Statistics, New York.
- [40] Price, K., Storn, M., and Lampinen, J., 2006, *Differential Evolution: A Practical Approach to Global Optimization*, Springer Science & Business Media, Berlin.